Human Molecular Genetics, 2018, Vol. 27, No. 15 2725–2738

doi: 10.1093/hmg/ddy182
Advance Access Publication Date: 16 May 2018
Original Article

ORIGINAL ARTICLE

Fingolimod phosphate inhibits astrocyte inflammatory activity in mucolipidosis IV

Laura D. Weinstock[1], Amanda M. Furness[2], Shawn S. Herron[2], Sierra S. Smith[2], Sitara B. Sankar[1], Samantha G. DeRosa[2], Dadi Gao[2], Molly E. Mepyans[2], Anna Scotto Rosato[3], Diego L. Medina[3], Ayelet Vardi[4], Natalia S. Ferreira[5], Soo Min Cho[4], Anthony H. Futerman[4], Susan A. Slaugenhaupt[2], Levi B. Wood[1,*,†] and Yulia Grishchuk[2,*,†]

[1]George W. Woodruff School of Mechanical Engineering, Wallace H. Coulter Department of Biomedical Engineering at Georgia Tech and Emory, Parker H. Petit Institute for Bioengineering & Bioscience, Georgia Institute of Technology, 315 Ferst Dr., 30332 Atlanta, GA, USA, [2]Department of Neurology, Center for Genomic Medicine, Massachusetts General Hospital Research Institute, Harvard Medical School, 185 Cambridge St., 02114 Boston, MA, USA, [3]Telethon Institute of Genetics and Medicine (TIGEM), via Campi Flegrei 34, 80078 Pozzuoli (NA), Italy, [4]Department of Biomolecular Sciences, Weizmann Institute of Science, Rehovot 76100, Israel and [5]Institute of Pharmacology and Toxicology, University of Zurich-Vetsuisse, Winterthurerstrasse 260, 8057 Zurich, Switzerland

* To whom correspondence should be addressed at: Tel: +1 404 3854465; Fax: 404-385-5965; Email: levi.wood@me.gatech.edu (L.B.W.); Tel: +1 6177260843; Fax: 617 726 5735; Email: ygrishchuk@partners.org (Y.G.)

Abstract

Mucolipidosis IV (MLIV) is an orphan neurodevelopmental disease that causes severe neurologic dysfunction and loss of vision. Currently there is no therapy for MLIV. It is caused by loss of function of the lysosomal channel mucolipin-1, also known as TRPML1. Knockout of the *Mcoln1* gene in a mouse model mirrors clinical and neuropathologic signs in humans. Using this model, we previously observed robust activation of microglia and astrocytes in early symptomatic stages of disease. Here we investigate the consequence of mucolipin-1 loss on astrocyte inflammatory activation *in vivo* and *in vitro* and apply a pharmacologic approach to restore *Mcoln1*$^{-/-}$ astrocyte homeostasis using a clinically approved immunomodulator, fingolimod. We found that *Mcoln1*$^{-/-}$ mice over-express numerous pro-inflammatory cytokines, some of which were also over-expressed in astrocyte cultures. Changes in the cytokine profile in *Mcoln1*$^{-/-}$ astrocytes are concomitant with changes in phospho-protein signaling, including activation of PI3K/Akt and MAPK pathways. Fingolimod promotes cytokine homeostasis, down-regulates signaling within the PI3K/Akt and MAPK pathways and restores the lysosomal compartment in *Mcoln1*$^{-/-}$ astrocytes. These data suggest that fingolimod is a promising candidate for preclinical evaluation in our MLIV mouse model, which, in case of success, can be rapidly translated into clinical trial.

[†]The last two authors contributed equally to this work.

Received: February 6, 2018. **Revised:** April 9, 2018. **Accepted:** May 8, 2018

Introduction

Mucolipidosis IV (MLIV) is a devastating neurologic childhood disease with a dramatic unmet medical need. At present, there is neither a specific treatment for MLIV nor a complete mechanistic model explaining its pathology. The neurologic symptoms usually appear during the first year of life and result in motor and cognitive deficiencies (1–5). Brain magnetic resonance imaging studies have revealed a dysgenic corpus callosum, impaired myelination in the white matter and decreased T2 signal intensities in the thalamus owing to increased ferritin deposition (6,7). The vast majority of MLIV patients are of Ashkenazi Jewish origin, with a carrier frequency in this population of about 1:100 (8). Despite the severity of the disease, human brain pathology data in MLIV are presently limited to two cases (2,3). The diagnostic ultrastructural hallmark of MLIV is the accumulation of storage bodies containing gangliosides, phospholipids and acidic mucopolysaccharides reported in every tissue, including the brain (3). The MLIV gene, *MCOLN1*, encodes a TRP family ion channel named mucolipin-1, or TRPML1 (9–12). There are more than twenty *MCOLN1* mutations associated with MLIV (5,8,13). The vast majority of MLIV cases (95% of Ashkenazi Jewish patients) result from a complete loss of mRNA and protein (11,14).

The MLIV mouse ($Mcoln1^{-/-}$) is an excellent phenotypic model of human MLIV enabling us to interrogate pathways affected by loss of TRPML1. All of the hallmarks of MLIV are present in $Mcoln1^{-/-}$ mice with the exception of corneal clouding (15–17). Defective myelination and gliosis, characteristic of human MLIV, are present in young adult mice at the onset of cognitive and motor deficits (16). However, activation of microglia and astrocytes was, surprisingly, not accompanied by neuronal loss in the regions with the most pronounced gliosis even at the late stage of disease. At the ultrastructural level, $Mcoln1^{-/-}$ astrocytes display large electron-dense inclusions with compact membranous and granular compartments that are characteristic of MLIV (16).

Therapy development is especially challenging in MLIV for a number of reasons. Since most MLIV patients do not have *MCOLN1* transcripts, chaperone therapy or pharmacologic enhancement of TRPML1 channel function are low-priority treatment approaches for MLIV. Other therapy approaches that are being successfully pursued for enzymatic lysosomal diseases, including infusion of recombinant protein, bone-marrow transplantation or gene-therapy, are based on cross-correction phenomena, and hold low or no promise in MLIV owing to transmembrane localization of TRPML1. Therefore, we believe that identifying and modulating the cellular pathways affected by loss of TRPML1 is a more tractable way to address the MLIV treatment challenge.

Astrocyte activation is a particularly attractive therapeutic target for MLIV since astrocytes are now recognized to play pathogenic roles in numerous neurodegenerative diseases (18,19). Moreover, astrocyte activation is a common feature of numerous lysosomal diseases with CNS impairment, including Niemann–Pick disease, neuronal ceroid lipofuscinosis (NCL) and multiple sulfatase deficiency (20–23). In juvenile NCL (CLN3 disease), astrocytes are functionally compromised and have been reported to have negative impact on neuronal survival and neurite morphology, demonstrating an active and detrimental role in CNS diseases (23).

Given that reactive astrocytosis is a key feature of the CNS pathology in MLIV and appears early in the course of the disease, we set out to test whether astrocyte dysfunction is a cell-autonomous component of MLIV and if targeting of astrocytes can promote homeostasis. Indeed, we found that $Mconl1^{-/-}$ astrocyte cultures autonomously reproduced the astrocyte inflammatory phenotype found in $Mcoln1^{-/-}$ mice. We treated $Mcoln1^{-/-}$ astrocytes with fingolimod, which is a Food and Drug Administration (FDA)-approved drug for remitting-relapsing multiple sclerosis that reduces astrocyte activation (24). Excitingly, fingolimod reduced both inflammatory signaling and cytokine expression and restored homeostatic expression of the lysosomal marker Lamp1. In total, our findings indicate that fingolimod promotes both inflammatory and lysosomal homeostasis in $Mcoln1^{-/-}$ astrocytes. Furthermore, since fingolimod is FDA-approved, and astrocytosis is an early component of MLIV pathology, fingolimod represents a highly promising and rapidly translatable therapy for this devastating childhood disease.

Results

Astrocyte activation and cytokine expression is up-regulated in the $Mcoln1^{-/-}$ mouse brain

Our group previously characterized the first genetic $Mcoln1^{-/-}$ mouse model of MLIV (15–17). We found that young adult (2-month-old) $Mcoln1^{-/-}$ mice demonstrated hypomylenation and activated microglia and astrocytes that were not accompanied by neuronal loss. These findings suggest that neuroinflammation plays an early, and potentially causal, role in disease pathogenesis. In order to further assess the role of neuroinflammation in this disease, we analyzed astrocyte activation in the cerebral cortex of $Mcoln1^{-/-}$ mice in early postnatal development (Fig. 1A). Using immunohistochemical staining (IHC) for the astrocyte activation marker glial fibrillary acidic protein (GFAP) we observed progressively increasing astrocyte activation beginning at P10 (Fig. 1B) indicating early postnatal onset of reactive astrocytosis. Importantly, neonatal mice (P1) displayed no sign of astrocyte activation. This shows that the early stages of postnatal brain development are particularly sensitive to the loss of *Mcoln1*. Interestingly, the activation of astrocytes in the cortex at postnatal day 10 is accompanied by deficient myelination as has been shown by our group previously (15).

To further characterize the inflammatory microenvironment in $Mcoln1^{-/-}$ brains, we next used a Luminex multiplexed immunoassay (Millipore) to quantify protein expression of 32 cytokines in the cortices of 2mo female $Mcoln1^{-/-}$ and $Mcoln1^{+/+}$ mice (Fig. 1C). To account for the multi-dimensional nature of the data, we used a discriminant partial least squares regression (D-PLSR) (25,26) to identify a weighted combination of cytokines, called a latent variable (LV1) that distinguished $Mcoln1^{-/-}$ and $Mcoln1^{+/+}$ mice (Fig. 1D). LV1 consisted of a *profile* of cytokines that were most differentially expressed between $Mcoln1^{-/-}$ and $Mcoln1^{+/+}$mice (Fig. 1E). Error bars [Fig. 1E, mean ± standard deviation (SD)] generated via a leave-one-out cross-validation (LOOCV) suggest that the involvement of any one cytokine in the profile was not owing to just a single sample (note that in contrast to these LOOCV plots, error bars are presented as mean ± standard error of mean (SEM) in bar plots used to compare differences between genotypes and conditions). Based on the profile, LV1, we observed significant difference between genotypes (Fig. 1F). Moreover, the profile identified numerous pro-inflammatory cytokines up-regulated in $Mcoln1^{-/-}$ mice, including IP-10, IL-17, Eotaxin and KC (Fig. 1G). These cytokines are known to be secreted by activated astrocytes (27–33) and to promote microglial activation

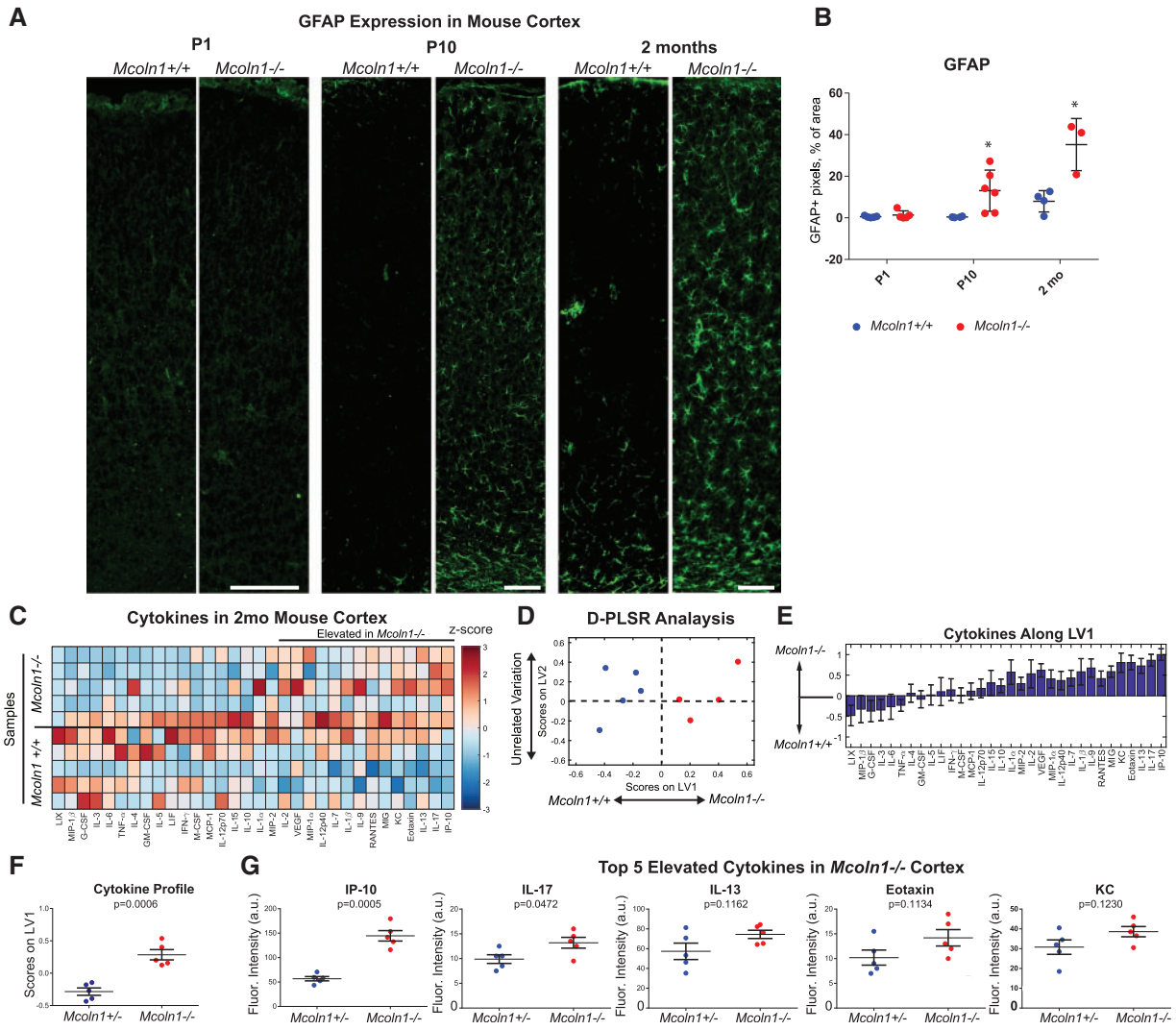

Figure 1. Astrocytes are highly reactive in *Mcoln1*$^{-/-}$ mice. (**A**) Immunohistochemistry for cortical GFAP expression in *Mcoln1*$^{-/-}$ mice and wild-type *Mcoln1*$^{+/+}$ controls. Scale bar = 100 μm. (**B**) GFAP expression (shown as % of positive area for individual mice) is increased in *Mcoln1*$^{-/-}$ mice after postnatal day (P) 10; P1: $n = 5$ *Mcoln1*$^{+/+}$ and 5 *Mcoln1*$^{-/-}$; P10: $n = 4$ *Mcoln1*$^{+/+}$ and 6 *Mcoln1*$^{-/-}$; and 2 mo: $n = 4$ *Mcoln1*$^{+/+}$ and 3 *Mcoln1*$^{-/-}$. *P-value <0.05 (mean ± SEM; two-tailed *t*-test). (**C**) Multiplexed Luminex analysis of 32 cytokines expressed in the cortex reveals differences in cytokine expression between *Mcoln1*$^{-/-}$ and *Mcoln1*$^{+/+}$ controls (z-scored). (**D**) A multivariate D-PLSR identified an axis in the cytokine data called a LV1 that distinguished *Mcoln1*$^{-/-}$ from *Mcoln1*$^{+/+}$ mice. (**E**) The separating axis, LV1, consisted of a profile of cytokines that correlated with *Mcoln1*$^{-/-}$ (positive) or *Mcoln1*$^{+/+}$ (negative) mice (error bars represent mean ± SD across LV1 generated for all models in a LOOCV). (**F**) Plotting each sample in terms of its overall cytokine score on LV1 revealed a significant difference in cytokine expression between *Mcoln1*$^{-/-}$ and *Mcoln1*$^{+/+}$ mice (two-tailed *t*-test, mean ± SEM). (**G**) Individually plotting the top five correlates from LV1 identified some significant individual differences (mean ± SEM; two-tailed *t*-test).

(28,29,34–37) and firmly demonstrate pro-inflammatory signaling as an early component of MLIV pathogenesis.

Inflammatory cytokine expression is increased in astrocyte cell cultures from *Mcoln1*$^{-/-}$ mice

Based on our analysis of astrocyte activation and cytokine expression in cortical tissues of young *Mcoln1*$^{-/-}$mice (Fig. 1), we next investigated whether pro-inflammatory astrocyte activation is a cell-autonomous function in MLIV, i.e. caused by intrinsic pathway dysregulation owing to loss of *Mcoln1*. To test this, we generated cortical primary astrocyte cultures from neonatal *Mcoln1*$^{-/-}$ knockout and control mice to determine if *Mcoln1*$^{-/-}$ astrocytes were constitutively activated. For controls in this study, we used *Mcoln1*$^{+/-}$ astrocytes, since human carriers are asymptomatic (11) and heterozygous mice display no disease phenotype (unpublished observations).

We used cytokine secretion as a robust measure of astrocyte pro-inflammatory activation *in vitro*. To detect differences in cytokine secretion, *Mcoln1*$^{-/-}$ and *Mcoln1*$^{+/-}$ astrocytes were cultured for 24 h in freshly changed culture medium. We quantified relative concentrations of 32 cytokines using Luminex analysis (Fig. 2A) and used a D-PLSR to identify an axis of cytokines, LV1, that best distinguished *Mcoln1*$^{-/-}$ from *Mcoln1*$^{+/-}$ conditioned media (Fig. 2B). LV1 identified a profile of cytokines that positively correlated with *Mcoln1*$^{-/-}$ samples (Fig. 2C). Plotting individual samples along LV1 showed that this profile of cytokines was significantly different in *Mcoln1*$^{-/-}$ astrocytic culture (Fig. 2D). Furthermore, plotting individual top positively and negatively correlated cytokines demonstrated significant expression differences in certain chemokines in *Mcoln1*$^{-/-}$ cultures (Fig. 2E). Interestingly only certain cytokines were up-regulated in *Mcoln1*$^{-/-}$ astrocytes, whereas control astrocytes exposed to a physiologically relevant

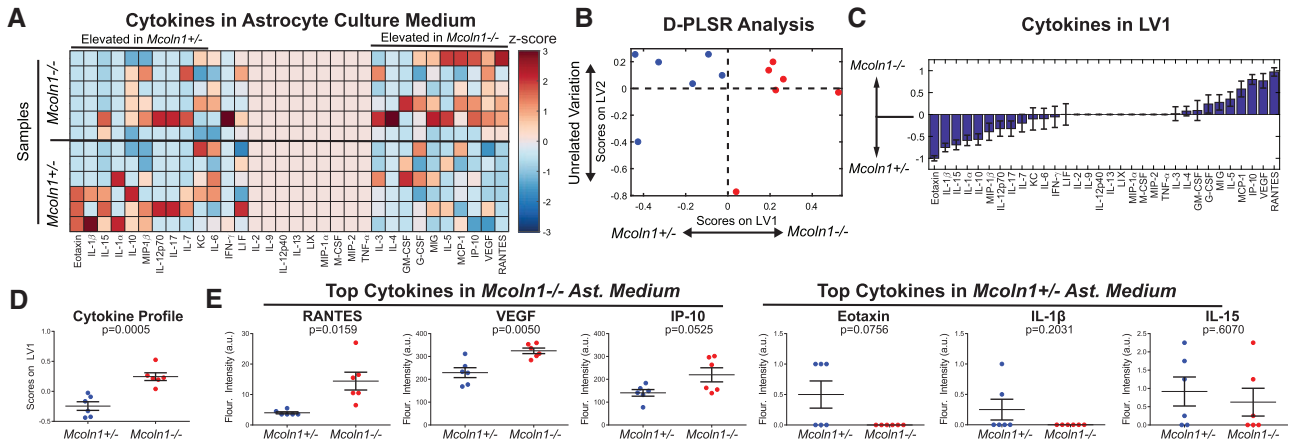

Figure 2. Dysregulated secretion of cytokines and chemokines in primary *Mcoln1*$^{-/-}$ astrocyte culture. (**A**) Luminex analysis of 32 cytokines secreted into the medium from *Mcoln1*$^{-/-}$ and control *Mcoln1*$^{+/-}$ astrocyte cell cultures 24 h after a medium refresh (z-score). (**B**) D-PLSR analysis of cytokines identified an axis (LV1) that distinguishes *Mcoln1*$^{-/-}$ and *Mcoln1*$^{+/-}$ astrocytes. (**C**) LV1 consists of a profile of cytokines that correlate with *Mcoln1*$^{-/-}$ (positive) or *Mcoln1*$^{+/-}$ (negative) astrocytes (mean ± SD across LV1 generated for all models in a LOOCV). (**D**) Plotting individual medium samples on the cytokine *profile* LV1 demonstrates that cytokine expression is significantly different between *Mcoln1*$^{-/-}$ and *Mcoln1*$^{+/-}$ astrocytes. (**E**) Expression of individual cytokines that most strongly correlate with *Mcoln1*$^{-/-}$ or *Mcoln1*$^{+/-}$ astrocytes illustrates differences in individual cytokines.

concentration of 50 nM amyloid β1–42 or 10 ng/ml IL-1β yielded increased production of all cytokines measured (Supplementary Material, Fig. S1). This result suggests that loss of TRPML1 produces an isolated change in astrocyte inflammatory activation that is distinct from the activation profile associated with gross pathogenic or pro-inflammatory stimulation. Importantly, certain cytokines up-regulated in *Mcoln1*$^{-/-}$ cultures overlapped with those up-regulated in *Mcoln1*$^{-/-}$ mouse cortices, including IP-10, RANTES and VEGF (Figs 1E and 2C). Given the known roles of these cytokines for stimulating microglial inflammatory activation (34,35,38–40), these data suggest that *Mcoln1*$^{-/-}$astrocytes have the capacity to broadly stimulate neuroinflammation in MLIV.

Mitogen-activated protein kinase and PI3K/Akt signaling are increased in *Mcoln1*$^{-/-}$ astrocytes

Our *in vivo* and *in vitro* analyses of astrocyte activation (Figs 1 and 2), in particular the fact that *Mcoln1*$^{-/-}$ astrocytes display a significantly altered profile of cytokine and chemokine secretion when cultured *in vitro*, suggest that *Mcoln1*$^{-/-}$ astrocytes are autonomously activated in MLIV. Since inflammation is regulated by intracellular signaling, we next quantified phospho-protein signaling within the mitogen-activated protein kinase (MAPK), Jak/STAT, and PI3K/Akt pathways using Luminex analysis (Fig. 3A). Changes in intracellular phospho-protein signaling occur on much faster time scales than resulting cellular phenotypes, such as protein synthesis and secretion of cytokines (41). Therefore, to sensitively detect genotype-specific differences in phospho-signaling between *Mcoln1*$^{-/-}$ and *Mcoln1*$^{+/-}$ astrocytes, we quantified signaling 5 min after refreshing the culture medium by using Luminex analysis of 21 signaling phosphoproteins (Fig. 3B). MAPK and PI3K/Akt signaling were dramatically increased in *Mcoln1*$^{-/-}$ astrocytes. Moreover, a D-PLSR analysis identified a specific *Mcoln1*$^{-/-}$ astrocyte phosphoprotein profile (Fig. 3C–E) that includes key signaling nodes within both the MAPK and PI3K/Akt pathways. Notably, phosphorylated p70S6K, GSK3α, Akt and RPS6, the top four proteins correlated with *Mcoln1*$^{-/-}$ astrocytes, are all in the PI3K/Akt pathway. Phospho-signaling in the MAPK pathway was also increased, including phospho-MSK1, -Jnk and -cJun (Fig. 3B). Finally, since these data suggest that PI3K/Akt pathway signaling plays an important role in *Mcoln1*$^{-/-}$ dysfunction, we quantified Akt phosphorylation in cortical and cerebellar lysates from mice that had been re-fed after withholding of chow for 22 h to synchronize signaling (42). Our *in vivo* data suggest increased Akt phosphorylation in *Mcoln1*$^{-/-}$ mice compared with controls (Supplementary Material, Fig. S2), indicating that our cell culture model reflects the *in vivo* condition.

Together, our data indicate that pro-inflammatory signaling is broadly increased via multiple pathways in *Mcoln1*$^{-/-}$ astrocytic cultures, providing evidence of defective signaling in astrocytes in MLIV. Broad dysregulation delineated by these data suggests that targeting individual pathways will be ineffective for restoring astrocyte homeostasis.

Transcriptome analysis of *Mcoln1*$^{-/-}$ astrocytes shows increased expression of the inflammation and metabolic networks

To gain a more detailed understanding of the pathways associated with astrocyte pro-inflammatory activation in MLIV, we next used RNA-seq analysis to quantify transcriptome-wide gene expression changes in *Mcoln1*$^{-/-}$ and *Mcoln1*$^{+/+}$ astrocyte cultures ($N = 4$). An initial hierarchical clustering demonstrated that one of the *Mcoln1*$^{+/+}$ samples was an outlier, and it was removed from subsequent analyses (Supplementary Material, Fig. S3A). From the remaining samples, we found 7700 gene transcripts to be measureable with normalized read counts greater than 10 for at least 1 sample (Supplementary Material, Fig. S3B). Of these, 97 genes were differentially expressed between *Mcoln1*$^{+/+}$ and *Mcoln1*$^{-/-}$ astrocytes (Fig. 4A; Supplementary Material, Fig. S3C and Tables S1 and S2). To thoroughly characterize altered pathways in *Mcoln1*$^{-/-}$ astrocytes, we conducted a gene set enrichment analysis (GSEA) (44) to identify pathways associated with differentially regulated genes. Of 3427 curated gene sets (see Materials and Methods section), the GSEA identified 570 significantly enriched gene sets in *Mcoln1*$^{-/-}$ and 114 significantly enriched gene sets in *Mcoln1*$^{+/+}$ astrocytes below the recommended false discovery rate (FDR) adjusted *P*-value threshold of 0.25 (44) (Fig. 4B and D; Supplementary Material, Table S3).

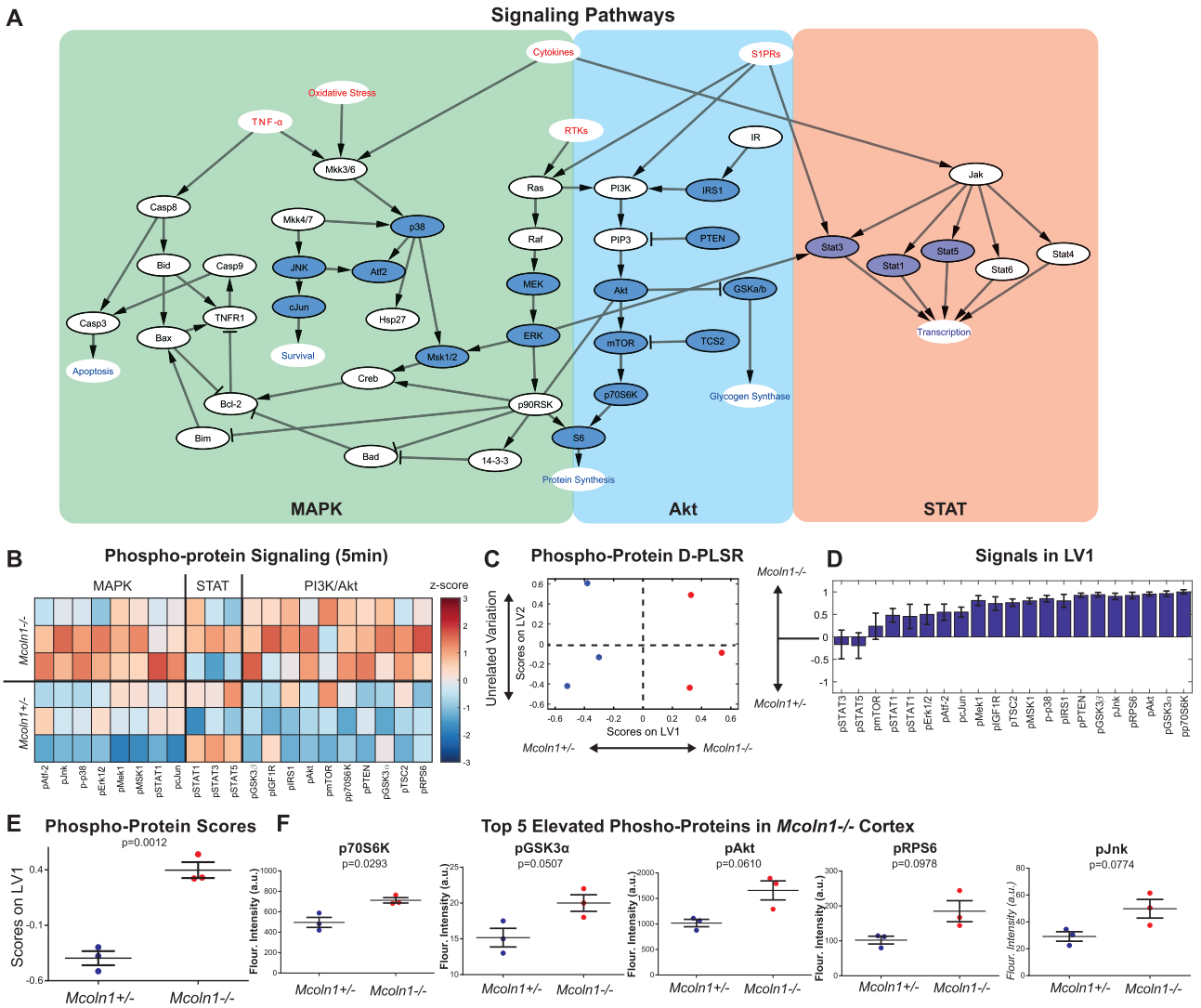

Figure 3. *Mcoln1*$^{-/-}$ astrocytes display activation of the MAPK and PI3K/Akt pathways. (**A**) Signaling network diagram depicting the interaction between phospho-proteins within the MAPK, Jak/Stat and PI3K/Akt pathways. Proteins labeled in blue are quantified via Luminex analysis. (**B**) Quantification of 21 phospho-proteins within the MAPK, Jak/Stat and PI3K/Akt pathways 5 min after a medium refresh. (**C**) D-PLSR analysis identified a phospho-protein signaling axis, LV1, that distinguished *Mcoln1*$^{-/-}$ and control *Mcoln1*$^{+/-}$ astrocytes. (**D**) LV1 consisted of a profile of phospho-proteins correlated with *Mcoln1*$^{-/-}$ or *Mcoln1*$^{+/-}$ astrocytes (mean ± SD in LOOCV). (**E**) Plotting individual samples on the signaling *profile* LV1 demonstrates that signaling is significantly different between *Mcoln1*$^{-/-}$ and *Mcoln1*$^{+/-}$ astrocytes (two-tailed *t*-test; mean ± SEM). (**F**) Several individual phospho-proteins within the PI3K/Akt and MAPK pathways have $P < 0.10$ (two-tailed *t*-test, mean ± SEM).

Importantly, our analysis identified significant up-regulation of inflammatory signaling through IL-6, IL-4 and Interferon-α and -β pathways in *Mcoln1*$^{-/-}$ astrocytes, with at least 30% of the detectable genes in these pathways enriched (Fig. 4D). Upregulation of these pathways is consistent with our cytokine-chemokine and phospho-protein signaling data and further indicates cell-autonomous pro-inflammatory activation of *Mcoln1*$^{-/-}$ astrocytes. We also noted significant changes in the sphingosine-1-phosphate (S1P) pathway (Fig. 4B and D), which is upstream of multiple pro-inflammatory pathways (Fig. 3A).

Interestingly, multiple pathways related to the metabolism of lipids and carbohydrates were also significantly over-represented in *Mcoln1*$^{-/-}$ astrocytes (Fig. 4B). GSEA analysis further identified that gene sets for astrocyte markers and aquaporin-mediated transport were also upregulated in *Mcoln1*$^{-/-}$ cells showing that ablation of *Mcoln1* expression results in core changes in astrocyte biology. Of interest, there were numerous pathways downregulated in *Mcoln1*$^{-/-}$ culture (enriched in *Mcoln1*$^{+/+}$) related to RNA-metabolism and protein synthesis and metabolism (Fig. 4C). This suggests inhibition of protein synthesis in *Mcoln1*$^{-/-}$ cells at multiple levels, including ribosomal function, translation and peptide elongation despite increased mTOR activity.

Taken together, our data show widespread dysregulation of multiple pathways in *Mcoln1*$^{-/-}$ astrocytes. Given this broad dysregulation, we next wanted to test whether targeting of the S1P pathway, which is upstream of inflammatory signaling affected in *Mcoln1*$^{-/-}$ astrocytes, will be sufficient to restore astrocyte homeostasis.

Fingolimod-phosphate inhibits elevated phospho-protein signaling in *Mcoln1*$^{-/-}$ astrocytes

Our cytokine data (Fig. 2) indicate that *Mcoln1*$^{-/-}$ astrocytes have increased expression of multiple pro-inflammatory and

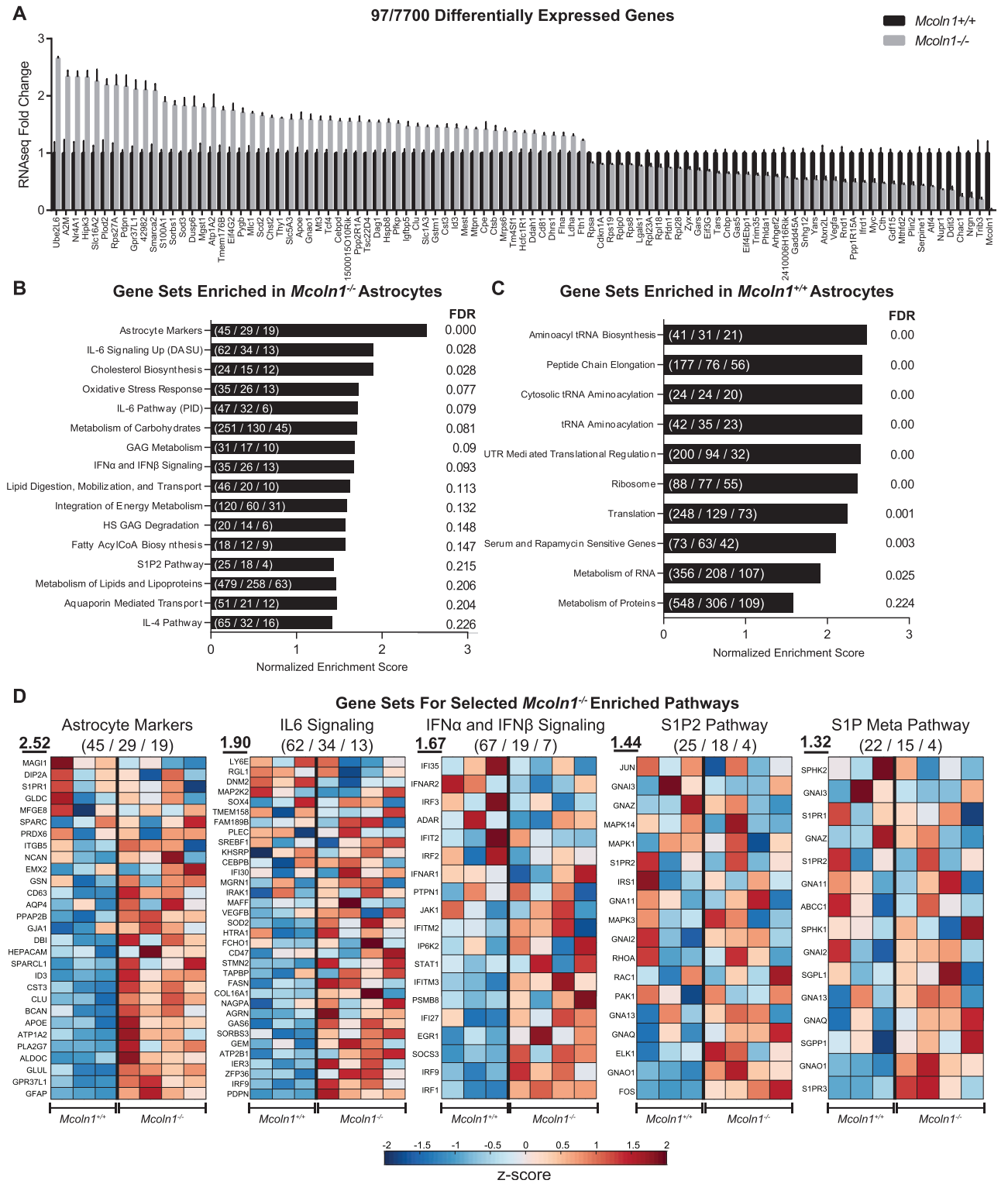

Figure 4. RNA-seq analysis shows that metabolic and pro-inflammatory signaling pathways are enriched in *Mcoln1*$^{-/-}$ astrocytes. (**A**) Mean fold-change values for 97 significantly differentially expressed genes (adjusted *P*-value <0.05) from RNA-seq analysis of *Mcoln1*$^{-/-}$ and *Mcoln1*$^{+/+}$ astrocytes normalized to the mean of the *Mcoln1*$^{-/-}$ expression values (adjusted *P*-values computed using R package `Dseq2`) (43) (mean ± SEM). Relevant gene sets enriched in (**B**) *Mcoln1*$^{-/-}$ or (**C**) *Mcoln*$^{+/+}$ astrocytes are ranked by normalized enrichment score from GSEA (bar magnitude). FDR adjusted *P*-value is displayed to the right of each bar. (**D**) Heatmaps display expression values for all selected genes within selected pathways. GSEA enrichment score is annotated in bold in the upper left of each panel (number of genes in pathway/number of genes detected/number of genes enriched; z-score).

chemotactic cytokines. While these cytokines reveal an important mechanism of astrocyte-mediated inflammatory signaling, they do not represent promising therapeutic targets owing to the lack of blood–brain barrier-permeable molecules that directly target cytokines and the non-specificity of such molecules. Importantly, our data also indicate strong up-regulation of multiple phospho-proteins in the MAPK and PI3K/Akt pathways in *Mcoln1*$^{-/-}$ astrocytes (Fig. 3) and in the S1P pathway (Fig. 4D), which is up-stream of both of these. These pathways regulate transcription of numerous pro-inflammatory factors, including cytokines. Thus, their broad dysregulation is likely promoting astrocyte inflammatory response and cytokine expression, leading to pro-inflammatory activation of microglia. Although specific blood–brain barrier permeable signaling inhibitors are available for targeting both MAPK and PI3K/Akt pathways, our observation that the two pro-inflammatory pathways are simultaneously up-regulated suggests that individual pathway suppression may not totally down-regulate cytokine expression. Interestingly, however, both MAPK and PI3K/Akt signaling are downstream of S1P (Fig. 3A) (24,45). Moreover, the pan-S1P receptor inhibitor, fingolimod (FTY720), has recently been approved to treat relapsing multiple sclerosis (46), and has been shown to down-regulate inflammatory activation of astrocytes (47,48). Therefore, we evaluated fingolimod in our astrocyte cultures to determine if it could suppress inflammatory signaling. Indeed, pre-treatment of astrocytes for 1 h with phospho-fingolimod (p-fing, the active form of the drug, 600 nM) significantly reduced MAPK and PI3K/Akt phosphorylation (Fig. 5A and B). Moreover, p-fingolimod treatment reduced expression of multiple pro-inflammatory cytokines that were up-regulated in *Mcoln1*$^{-/-}$ astrocytes (Figs. 2 and 5C and D). Interestingly, some chemokines, including RANTES, MCP-1 and neurotrophic factor VEGF (39) were resistant to fingolimod, while those with strong pro-inflammatory properties such as IP-10 and IL-6, were responsive to drug treatment. Our data indicate that p-fingolimod promotes inflammatory homeostasis in *Mcoln1*$^{-/-}$ astrocytes.

Fingolimod-phosphate attenuates expression of LAMP-1 in *Mcoln1*$^{-/-}$ astrocytes

Mcoln1 deficiency results in functional impairment and enlargement of lysosomes. Using electron microscopy in the *Mcoln1*$^{-/-}$ mouse brain, we have previously detected the presence of the large electron-dense inclusions with compact membranous and granular compartments in astrocytes, typical of MLIV (3,16). Structural and functional changes in the lysosomal compartment owing to *Mcoln1* loss can be monitored by increased immunoreactivity of the lysosomal marker lysosomal-associated membrane protein 1 (Lamp1) (49,50). Similarly, we detected increased expression of Lamp1 in our primary astrocytic culture derived from *Mcoln1*$^{-/-}$ mice (Fig. 6) as expressed by mean fluorescent intensity in GFAP-positive cells. Strikingly, our treatment with p-fingolimod (600 nM for 24 h) was able to significantly suppress the intensity of Lamp1 staining and suggests that fingolimod may potently correct lysosomal function, the primary cell pathology in MLIV.

Discussion

Though lysosomal inclusions are found in all organs and tissues of MLIV patients, CNS and eye dysfunction are the most debilitating aspects of the disease (4,51,52). The *Mcoln1*$^{-/-}$ mouse model has provided a detailed view of pathogenesis and suggests that astrocyte, microglial and oligodendrocyte dysfunction precedes neuronal damage. Astrocyte activation promotes pathogenesis in multiple neurodegenerative disease, both via their crosstalk with microglia and their direct neurotoxic effects via reactive oxygen species production and cytokine expression (18,19,53,54). We hypothesized that astrocyte dysfunction may be a cell-autonomous process in MLIV. Indeed, our data show that cultured *Mcoln1*$^{-/-}$ astrocytes possess increased signaling through multiple pro-inflammatory pathways and an abnormal lysosome.

Our data also show that cytokines upregulated in the mouse cortex, including IP-10, RANTES and VEGF are secreted by *Mcoln1*$^{-/-}$ astrocytes in culture (Figs 1 and 2). Incomplete overlap between cytokine/chemokine profiles in the mouse brain homogenates and media conditioned by astrocytes *in vitro* could be explained by the complexity of the brain tissue, as the chemokines and cytokines are produced by various brain cells, including astrocytes, neurons, microglia, brain endothelial cells and oligodendrocytes. In addition to this, our *in vitro* system allows us to measure only the factors secreted by the cells, whereas in brain homogenates we asses both intracellular and secreted levels. Interestingly, IP-10, RANTES and VEGF all recruit microglia in several diseases, including Alzheimer's disease (34,35,40,55–58). IP-10 is a pro-inflammatory cytokine primarily expressed by astrocytes (30) that triggers pro-inflammatory activation of microglia and may cause enhancement of brain-blood barrier permeability and myelin loss (28,34,59). Therefore, it is likely that astrocytes play a major role in promoting neuroinflammation and microglial activity in MLIV.

The success of the immunomodulatory drug fingolimod for treating recurring multiple sclerosis and its recently reported effect of reducing astrogliosis in epilepsy, stroke and multiple sclerosis models (46,47,60,61), shows its therapeutic potential for targeting neuroinflammation and neuroprotection (62,63). Moreover, fingolimod is a strong candidate for treating astrocytes in MLIV because our analysis of inflammation-mediating signaling shows that *Mcoln1*$^{-/-}$ astrocytes possess dysregulated signaling both within the S1P gene sets (Fig. 4D) and in multiple pathways (MAPK and PI3K/Akt), which are downstream of the S1P receptors that fingolimod targets (Fig. 3). Our finding that fingolimod-phosphate (the biologically active form of fingolimod) was able to suppress signaling in both of these pathways confirms its broad immunomodulatory potency for astrocytes.

Fingolimod targets S1P pathway, which is implicated in migration, differentiation, mitogenesis, apoptosis and inflammation (64). The S1P pathway consists of five G-protein coupled S1P receptors (S1PR1–S1PR5), each of which transduce signaling to different down-stream proteins, including through the PI3K/Akt and MAPK pathways reported here. Importantly, fingolimod is a functional antagonist of all 5 receptors, and drugs that target only a sub-set of these receptors do not possess immunomodulatory properties (24). While we have not directly quantified S1P, our transcriptomic analysis found that the S1P pathway was altered in *Mcoln1*$^{-/-}$ astrocytes (Fig. 4B and D). This, together with our demonstration that multiple downstream S1P pathways are dysregulated in MLIV, strongly suggests that fingolimod would improve astrocyte function.

Interestingly, despite broad suppression of MAPK and PI3K/Akt signaling, p-fingolimod only modulated some of the inflammatory cytokines over-expressed by *Mcoln1*$^{-/-}$ astrocyte cultures (e.g. IP-10, IL-6 and MIP-1β; Fig. 5B), while others were unchanged (e.g. RANTES, VEGF and MCP-1). Importantly, each of the modulated cytokines or chemokines have strong

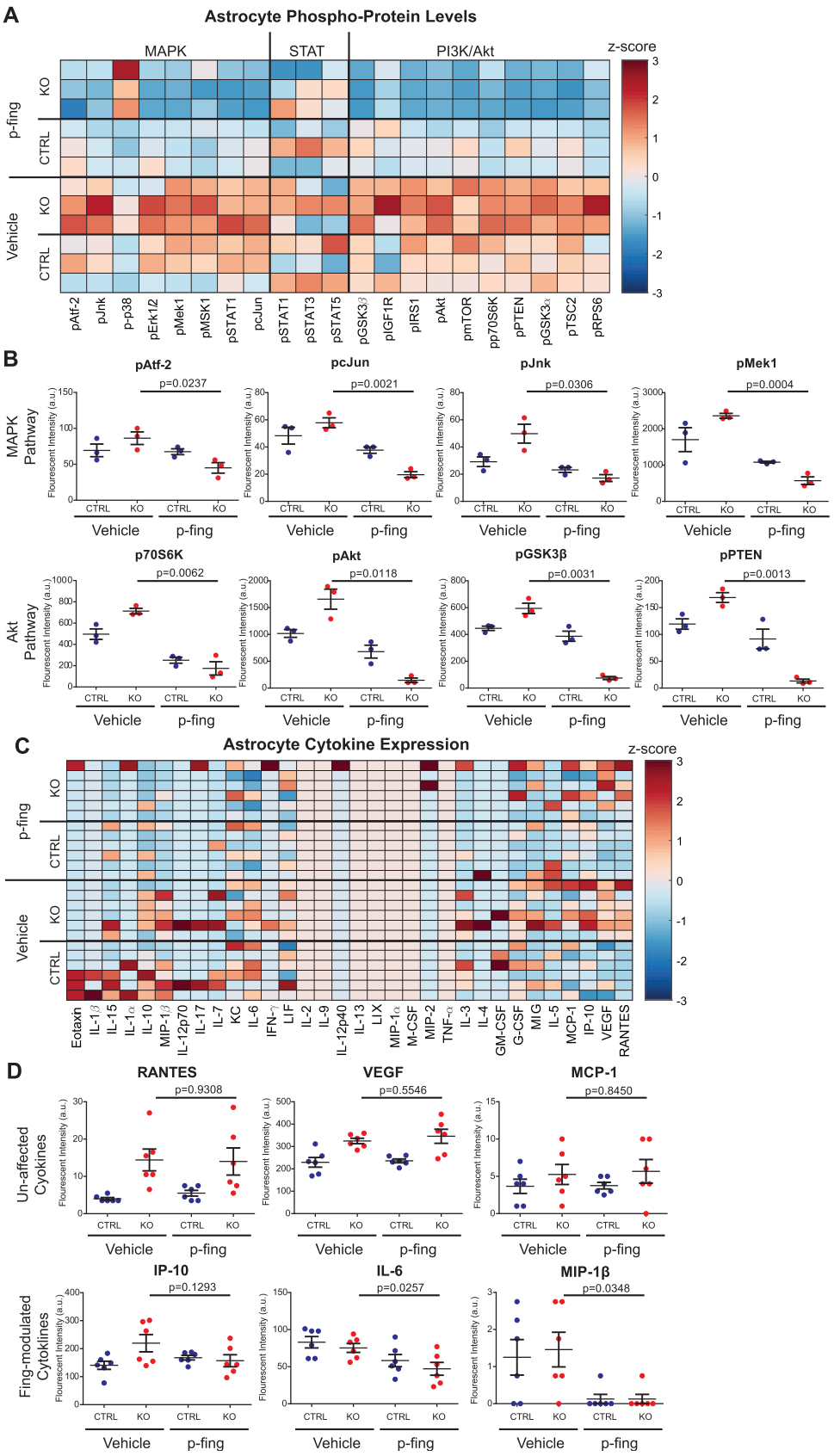

Figure 5. p-fing suppresses phospho-protein signaling in *Mcoln1*$^{-/-}$ astrocytes and reduces cytokine expression. (**A**) Luminex analysis of phospho-protein signaling at 5 min time point after 1 h pre-treatment with p-fing demonstrates broad down-regulation of signaling in the MAPK and PI3K/Akt pathways (z-score). (**B**) Multiple phospho-proteins in the PI3K/Akt and MAPK pathways were significantly suppressed in *Mcoln1*$^{-/-}$ astrocytes treated with p-fing (two-tailed *t*-test; mean ± SEM). (**C**) Luminex analysis of 32 cytokines quantified from *Mcoln1*$^{-/-}$ or *Mcoln1*$^{+/-}$ astrocytes treated with p-fing or vehicle (z-score); (**D**) p-fing treatment reduced astrocyte expression of certain pro-inflammatory cytokines (IP-10, IL-6, MIP-1β), and did not modulate others (RANTES, VEGF, MCP-1) (two-tailed *t*-test; mean ± SEM).

pro-inflammatory roles, while those that were not affected are primarily chemokines. One of the chemokines resistant to p-fingolimod treatment is a neurotrophic factor VEGF (39). Lack of its suppression by p-fingolimod in *Mcoln1*$^{-/-}$ astrocytes may be an important part of the neuroprotective action of fingolimod. Although showing only a modest trend in suppressing IP-10 in our data (Fig. 5D), the effect of fingolimod to suppress IP-10 has been also demonstrated in an *in vivo* model of traumatic brain injury model and in human primary astrocytes (62,65).

In addition to inflammatory and signaling differences, *Mcoln1*$^{-/-}$ astrocytes reproduced defective Lamp1 staining of lysosomes (Fig. 6). Excitingly, p-fingolimod suppressed Lamp1-positive immunoreactivity in *Mcoln1*$^{-/-}$ cells, which may suggest a restoration of lysosomal homeostasis. Note that morphologic assessment does not entirely prove the functional recovery of lysosomes in our experiments since we did not perform any functional assessment. The effects of fingolimod on lysosomal function have not previously been reported. However, mTOR is a strong regulator of lysosomal activity (66). Thus, one possible mechanism for the positive effect of p-fingolimod on lysosomal function is via inhibition of the PI3K/Akt pathway, including mTOR (Fig. 5). Mucolipin-1 is known to be a key regulator, and also a target, of mTOR signaling (67–70). Therefore, the fact that inhibition of mTOR by p-fingolimod resulted in reversal of the lysosomal phenotype in the absence of mucolipin-1 is intriguing and may indicate unknown mucolipin-1-independent compensatory mechanisms of mTOR regulation of lysosomal function. Since dysfunctional lysosomes are the key pathologic hallmark of MLIV in humans and mice, this result suggests that fingolimod restores homeostasis of multiple functional components affected in MLIV.

Fingolimod has been used in 93 clinical trials for multiple sclerosis and other diseases (www.Clinicaltrials.com). It is currently in trials for acute stroke (NCT02002390), astrocytoma (NCT02490930), ALS (NCT01786174), schizophrenia (NCT01779700), Rett syndrome (NCT02061137) and multiple sclerosis (NCT01892722). Importantly, the latter two are pediatric trials. These studies are anticipated to provide extensive safety data for various age groups and extend the list of indications. Given the growing evidence of the role of neuroinflammation in CNS dysfunction and disease (71,72), it is likely that fingolimod may prove effective in other rare genetic conditions such as MLIV. A recent study reported that fingolimod was beneficial in mouse models for two forms of NCL, CLN1 and CLN3 (73,74). Administration of fingolimod reduced microgliosis and infiltration of T cells into the CNS and attenuated axonal damage and neuronal death in the brain and retina in both models. This exciting result highlights the promise of employing immunomodulation for the treatment of lysosomal diseases, including MLIV. Our future work will be focused on pre-clinical testing of fingolimod in our *Mcoln1*$^{-/-}$ mouse model of MLIV, where the effect on astrocyte and microglia activation, levels of brain cytokines and chemokines and other hallmarks of MLIV neuropathology will be measured.

In summary, our data show that *Mcoln1*$^{-/-}$ astrocytes show broad signaling dysregulation. Moreover, these defects in signaling are associated with elevated expression of pro-inflammatory cytokines which likely promote MLIV pathogenesis. Excitingly, p-fingolimod was highly effective at restoring intracellular signaling, cytokine secretion and lysosomal function in *Mcoln1*$^{-/-}$ astrocytes. Since fingolimod is already FDA-approved for MS, our data suggest it can be a rapidly translatable therapeutic strategy for this devastating childhood disease.

Materials and Methods

Animals

Mcoln1 knock-out mice (on a C57Bl/6J background) were maintained and genotyped as described previously (17). *Mcoln1*$^{-/-}$ and *Mcoln1*$^{-/+}$ mouse pups for astrocytic cultures were generated from *Mcoln1*$^{-/+}$ and *Mcoln1*$^{-/-}$ mating. Littermate mice (*Mcoln1*$^{+/+}$ or *Mcoln1*$^{+/-}$) were used as controls for all experiments. CD-1 mice for the amyloid β1–42 conditioning experiment were purchased from Charles River. All experiments were performed according to the US National Institute of Health guidelines and approved by the Massachusetts General Hospital or the Georgia Institute of Technology Institutional Animal Care and Use Committee.

Astrocyte cultures

Neonatal littermate *Mcoln1*$^{-/-}$ and *Mcoln1*$^{-/+}$, or CD-1, pups (post-natal days 1–3) were euthanized by decapitation and tail snips were collected for genotyping. Brains were harvested, cortices isolated and meninges removed. The cortical tissue was homogenized via trituration and then transferred to poly-L-lysine (PLL) coated T25 cell culture flasks. The next day, flasks were knocked and media was exchanged to remove unwanted debris or residual tissue. Cells were grown to confluency (5–7 days), then placed on a shaker at 250 rpm for 18 h at 37°C to eliminate OPCs and microglia. After shaking the media was aspirated to remove the detached non-astrocytic cells, and the flask was rinsed with phosphate buffered saline (PBS). Astrocytes were detached from the bottom of the flask by trypsin; cells were counted and seeded in cell culture plates. For cytokine/chemokine and phosphoprotein assays, cells were seeded in six-well plates at 120 000 cells per well. Wild-type CD-1 astrocytes were used for analysis of cytokine expression in response to amyloid β1–42 in a vehicle of 0.001% NH_4OH (rPeptide, Bogart, GA, USA). For immunocytochemistry, cells were seeded on 12 mm PLL-pre-coated glass coverslips in 24-well plates at 30 000 cells per slip. After confluency was established (6–7 days) media was aspirated and replaced with 1 ml per well of either basal culture media or supplemented with 600 nM fingolimod phosphate for either 5 minutes or 24 h. Treatment was quenched with a cold PBS wash, conditioned media was collected, cells were lysed using the Bio-Plex Cell Lysis Kit (Bio-Rad, Hercules, CA, USA), scraped and lysates collected for analysis. For microscopy, cells seeded on glass coverslips were cultured for 6 days and were then treated with 300 μl of either base media or 600 nM fingolimod phosphate for 24 h. Treatment was quenched using cold PBS and slips were fixed in 4% PFA for 10 min on ice. Slips were rinsed and stored in PBS for future staining.

Luminex multiplexed immunoassays for cytokine and phospho-protein detection

Astrocyte media and cell lysates were stored at −80°C. For cytokine analysis, samples were diluted to 20% in Milliplex assay buffer and analyzed using the Milliplex MAP Mouse Cytokine/Chemokine Multiplex assay (Millipore Sigma, St. Louis, MO, USA, MCYTMAG-70K-PX32). Protein concentration was determined using Pierce bovine serum albumin (BSA) Protein Assay kit (ThermoFisher Scientific, Waltham, MA, USA). Protein concentration was normalized in Bio-Plex lysis buffer (Bio-Rad) to 0.15 μg for the STAT Cell Signaling 5-Plex Multiplex assay

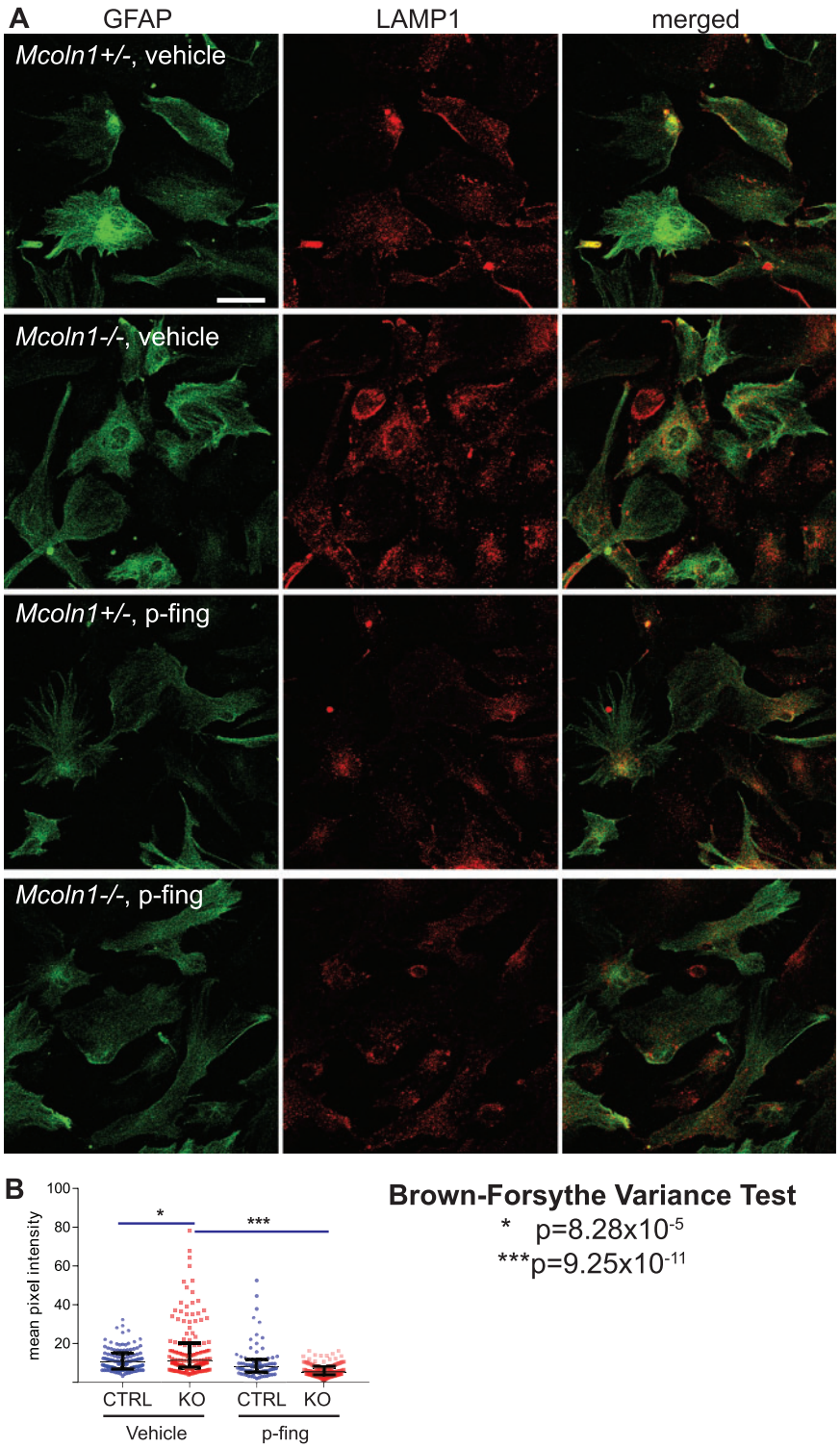

Figure 6. Lysosomal correction by p-fingolimod in *Mcoln1*$^{-/-}$ astrocytes. (**A**) Representative images of *Mcoln1*$^{-/+}$ *and Mcoln1*$^{-/-}$ astrocytic cultures immunostained for astrocytic marker GFAP (green) and lysosomal marker Lamp1 (red) treated with either p-fingolimod or vehicle for 24 h. Scale bar = 50 μm. (**B**) Lamp1 immunoreactivity is significantly increased in *Mcoln1*$^{-/-}$ cells when compared with *Mcoln1*$^{+/-}$ controls showing impaired lysosomal content and morphology. p-Fingolimod treatment significantly reduced Lamp-1 immunoreactivity in *Mcoln1*$^{-/-}$ astrocytes. Lamp1 immunoreactivity is expressed as mean pixel intensity, values for individual cells ($n = 116$, *Mcoln1*$^{+/-}$ vehicle; $n = 141$ *Mcoln1*$^{-/-}$ vehicle; $n = 80$, *Mcoln1*$^{+/-}$ p-fingolimod; $n = 154$, *Mcoln1*$^{-/-}$ p-fingolimod) and median values with interquartile range (black bars) are shown. *P*-values were computed using the Brown–Forsythe variance test, demonstrating significant difference in the variance between groups.

(Millipore Sigma, 48-610MAG), to 0.5 μg for the MAPK/SAPK Signaling 10-Plex Multiplex assay (Millipore Sigma, 48-660MAG) and to 0.4 μg for the Akt/mTOR Phosphoprotein Multiplex assay (Millipore Sigma, 48-611MAG). Phosphorylation sites for the MAPK/SAPK as follows: ATF2 (Thr71), Erk (Thr185/Tyr187), HSP27* (Ser78), JNK (Thr183/Tyr185), c-Jun (Ser73), MEK1 (Ser222), MSK1 (Ser212), p38 (Thr180/Tyr182), p53* (Ser15) and STAT1 (Tyr707). Akt/mTOR phospho-sites are: Akt (Ser473), GSK3α (Ser21), GSK3β (Ser9), IGF1R (Tyr1135/Tyr1136), IR* (Tyr1162/Tyr1163), IRS1* (Ser312), mTOR (Ser2448), p70S6K (Thr412), PTEN (Ser380), RPS6 (Ser235/Ser236) and TSC2 (Ser939). STAT kit phosphorylation sites are: STAT1 (Tyr701), STAT2* (Tyr690), STAT3 (Tyr705), STAT5A/B (Tyr694/699) and STAT6* (Tyr641) (available in Millipore Sigma Milliplex Analyte Quarterly, Vol. 2, 2017). Analytes marked with an asterisk have not been reported to be mouse-reactive and were removed from the analysis. Assays were read out with a MAGPIX Luminex instrument (Luminex, Austin, TX, USA).

Partial least squares modeling

D-PLSRs were performed in MATLAB using the PLS function written by Cleiton Nunes (available on the MathWorks File Exchange). The data were z-scored before being input into the PLS script. D-PLSRs were run individually for each Luminex assay. Phospho-proteins or cytokine measurements were used as the independent variables, and the discrete regression variable in all analyses was astrocyte treatment condition. Orthogonal rotations were applied to the sample scores and analyte weightings to obtain consistent separation of each group along the LV1 and LV2 axes. Error bars for LV loadings were calculated by iteratively excluding samples without replacement 1000 times, and regenerating the D-PLSR model each time. Error bars in the LV1 plots report the mean and SD computed across the models generated to provide an indication of the variability within each cytokine or phospho-protein among models.

Immunocytochemistry and image analysis

Fixed cells were blocked in 1% BSA (Gibco by ThermoFisher Scientific), 2% normal goat serum (Vector Laboratories, Burlingame, CA, USA) and 0.05% Saponin (Millipore Sigma) in PBS at room temperature for 5 min. Cells were then stained using primary antibodies against GFAP (mouse, 1:1000; 3670S, Cell Signaling Technology, Danvers, MA, USA) and LAMP1 (rat, 1:1000; 553 792; BD Pharmingen, San Jose, CA, USA) in blocking buffer for 90 min at room temperature. Cells were washed three times in 1% BSA in PBS and then stained with secondary antibodies goat anti-mouse AlexaFluor488 (1:1000; Invitrogen, Eugene, OR, USA) and goat anti-ratAlexaFluor633 (1:1000; Invitrogen) for 1 h at room temperature. Cells were again washed and then mounted on glass slides using Immumount (ThermoFisher Scientific). Cells were imaged using a Leica TCS SP5 confocal laser scanning microscope (Leica Microsystems, Inc., Wetzlar, Germany) with a 20× dry objective. Cells were imaged in Z-stacks with 1 μm intervals and Z-sections with the biggest cell surface area were included in analysis. Images were analyzed using FIJI software (NIH, Bethesda, MD, USA). Selections [region of interests (ROIs)] were made by tracing GFAP positive cells. All present GFAP+ cells within six to seven fields of view per genotype/treatment group were included in analysis. All images were thresholded using the same settings and mean pixel intensity of LAMP1 staining for all GFAP+ cells ($n = 116$, *Mcoln1*$^{+/-}$ vehicle; $n = 141$ *Mcoln1*$^{-/-}$ vehicle; $n = 80$, *Mcoln1*$^{+/-}$ p-fingolimod; $n = 154$, *Mcoln1*$^{-/-}$ p-fingolimod) was measured. Normality of the datasets was analyzed using D'Agostino and Pearson normality test using GraphPad Prizm 7 software (GraphPad, La Jolla, CA, USA). Lamp1 staining was primarily different in distribution, rather than mean, therefore, we compared Lamp1 staining for using the Brown-Forsythe variance test using `vartestn` in MATLAB.

Immunohistochemistry, imaging and analysis

Brain tissues for histologic analysis were obtained from P1, P10 and 2-month-old *Mcoln1*$^{-/-}$ and *Mcoln1*$^{+/+}$ mice. Brains were fixed in 4% PFA for 24 h, washed with PBS, cryoprotected in 30% sucrose, frozen in isopentane, and stored at −80°C until sectioned. For the P1 and P10 tissues, 20 μm thick coronal sections were made using a Cryostat and directly adhered to glass slides. Slides were allowed to dry completely overnight at room temperature, and sections were outlined with Dako Pen (Agilent, Santa Clara, CA, USA). Antigen retrieval was achieved by microwaving the slides 18 min, low power, in citrate buffer (10 mM citric acid and 0.05% Tween 20, pH 6.0). Slides were washed with PBS and then incubated for 1 h at room temperature with blocking buffer (0.5% Triton X-100, 5% normal goat serum in PBS). Primary anti-GFAP antibodies (mouse, 1:1000; 3670S; Cell Signaling Technology) in 1% NGS in PBS were applied and incubated overnight at 4°C. The next day, slides were incubated with secondary donkey anti-mouse AlexaFluor 488 antibodies (1:500; Invitrogen) for 90 min at room temperature, washed and mounted with Immumount (ThermoFisher Scientific). The brains from 2-month-old mice were serially sectioned at 40 μm thickness and stored free-floating in 96-well plates with TBSAF (TBS, 30% ethylene glycol, 15% sucrose and 0.05% sodium azide) at −80°C. GFAP immunostaining was done according to the protocol above adopted for free-floating sections.

The cortex region of each section was imaged on a Leica DMi8 epifluorescent microscope with at 10× dry objective. Images were the processed using FIJI (NIH). Regions of primary somatosensory and primary and secondary motor cortex were selected on each image, equally thresholded, and GFAP immunoreactivity was measured and expressed as percent of positive pixels from each selection. Comparisons between genotype groups were made using unpaired *t*-test in GraphPad Prizm 7 software (GraphPad).

RNA isolation and sequencing details

For RNA-seq, astrocyte pellets were collected and stored at -80°C. Total RNA was prepared using an RNeasy mini kit (Qiagen GmbH, Hilden, Germany) according to the manufacturer's guidelines, which included DNase treatment. We used a modification of MARSseq (75) for the generation of RNA-seq libraries. RNA-seq libraries were sequenced using Illumina NextSeq-500. Adaptors and low-quality bases were removed from the raw reads by *cutadapt* (76) and the remaining reads were mapped to the *Mus musculus* genome (mm10) using STAR v2.4.2a (77) with the option alignEndsType EndToEnd, and only the reads with unique mapping were considered for further analysis. Gene expression levels were calculated using htseq-count (78) with the option *intersecsion-strict* and mm10 Refseq 3′UTR GRF annotations. Normalization and differential expression analysis were performed using the DESeq2 R-package (Bioconductor, https://bioconductor.org/packages/release/bioc/html/DESeq2.html).

Transcriptome analysis

Genes measured by RNA-seq were normalized using DESeq2 R-package and only genes with 10 or more normalized reads for at least one sample were selected for analysis. Differentially expressed genes were defined as genes that had significant adjusted P-value <0.05. GSEA (44,79) was run using the MLIV astrocyte RNA-seq data and the full curated pathways list version 6.1 (cp2 v6.1 available at software.broadinstitute.org/gsea) with gene-set permutations. As recommended GSEA was conducted using human annotated gene sets. Mouse gene names were converted to upper case nomenclature to match human gene symbols and input to the GSEA software. Pathways above 0.25 FDR were considered significantly enriched (44,79). The accompanying heatmaps (generated using MATLAB) show normalized expression values for the genes in our dataset that fall in select enriched pathways.

Supplementary Material

Supplementary Material is available at *HMG* online.

Acknowledgements

The authors are thankful to the ML4 Foundation and particularly Rebecca Oberman, Ph.D., the executive director, for support, engagement in research, building of the ML4 research community and promoting the collaborative spirit of our work.

Conflict of Interest statement. None declared.

Funding

This work was supported in part by a grant from the ML4 foundation (to Y.G.) and by startup funds from the Georgia W. Woodruff School of Mechanical Engineering at the Georgia Institute of Technology (to L.B.W.). L.D.W. was supported in part by the National Institutes of Health Cell and Tissue Engineering Biotechnology Training Grant (T32-GM008433).

References

1. Crandall, B.F., Philippart, M., Brown, W.J. and Bluestone, D.A. (1982) Mucolipidosis IV. *Am. J. Med. Genet.*, **12**, 301–308.
2. Folkerth, R.D., Joseph Alroy, D.V.M., Lomakina, I., Skutelsky, E., Raghavan, S.S. and Kolodny, E.H. (1995) Mucolipidosis IV: morphology and histochemistry of an autopsy case. *J. Neuropathol. Exp. Neurol.*, **54**, 154–164.
3. Tellez-Nagel, I.R.I., Iwamoto, T., Johnson, A.B., Norton, W.T. and Nitowsky, H. (1976) Mucolipidosis IV. Clinical, ultrastructural, histochemical, and chemical studies of a case, including a brain biopsy. *Arch. Neurol.*, **33**, 828–835.
4. Chitayat, D., Meunier, C.M., Hodgkinson, K.A., Silver, K., Flanders, M., Anderson, I.J., Little, J.M., Whiteman, D.A. and Carpenter, S. (1991) Mucolipidosis type IV: clinical manifestations and natural history. *Am. J. Med. Genet.*, **41**, 313–318.
5. Wakabayashi, K., Gustafson, A.M., Sidransky, E. and Goldin, E. (2011) Mucolipidosis type IV: an update. *Mol. Genet. Metab.*, **104**, 206–213.
6. Bonavita, S., Virta, A., Jeffries, N., Goldin, E., Tedeschi, G. and Schiffmann, R. (2003) Diffuse neuroaxonal involvement in mucolipidosis IV as assessed by proton magnetic resonance spectroscopic imaging. *J. Child Neurol.*, **18**, 443–449.
7. Frei, K.P., Patronas, N.J., Crutchfield, K.E., Altarescu, G. and Schiffmann, R. (1998) Mucolipidosis type IV: characteristic MRI findings. *Neurology*, **51**, 565–569.
8. Altarescu, G., Sun, M., Moore, D.F., Smith, J.A., Wiggs, E.A., Solomon, B.I., Patronas, N.J., Frei, K.P., Gupta, S., Kaneski, C.R. *et al.* (2002) The neurogenetics of mucolipidosis type IV. *Neurology*, **59**, 306–313.
9. Colletti, G.A. and Kiselyov, K. (2011) Trpml1. *Adv. Exp. Med. Biol.*, **704**, 209–219.
10. Bach, G. (2005) Mucolipin 1: endocytosis and cation channel—a review. *Pflugers Arch.*, **451**, 313–317.
11. Slaugenhaupt, S.A., Acierno, J.S., Jr, Helbling, L.A., Bove, C., Goldin, E., Bach, G., Schiffmann, R. and Gusella, J.F. (1999) Mapping of the mucolipidosis type IV gene to chromosome 19p and definition of founder haplotypes. *Am. J. Hum. Genet.*, **65**, 773–778.
12. Bargal, R., Avidan, N., Ben-Asher, E., Olender, Z., Zeigler, M., Frumkin, A., Raas-Rothschild, A., Glusman, G., Lancet, D. and Bach, G. (2000) Identification of the gene causing mucolipidosis type IV. *Nat. Genet.*, **26**, 118–123.
13. Schiffmann, R., Grishchuk, Y. and Goldin, E. (1993) Mucolipidosis IV. In Adam, M.P., Ardinger, H.H., Pagon, R.A., Wallace, S.E., Bean, L.J.H., Stephens, K. and Amemiya, A. (eds), *GeneReviews®* [Internet]. University of Washington, Seattle, 1993–2018.
14. Slaugenhaupt, S.A. (2002) The molecular basis of mucolipidosis type IV. *Curr. Mol. Med.*, **2**, 445–450.
15. Grishchuk, Y., Pena, K.A., Coblentz, J., King, V.E., Humphrey, D.M., Wang, S.L., Kiselyov, K.I. and Slaugenhaupt, S.A. (2015) Impaired myelination and reduced ferric iron in mucolipidosis IV brain. *Dis. Model. Mech.*, **8**, 1591–1601.
16. Grishchuk, Y., Sri, S., Rudinskiy, N., Ma, W., Stember, K.G., Cottle, M.W., Sapp, E., Difiglia, M., Muzikansky, A. and Betensky, R.A. (2014) Behavioral deficits, early gliosis, dysmyelination and synaptic dysfunction in a mouse model of mucolipidosis IV. *Acta Neuropathol.*, **2**, 133.
17. Venugopal, B., Browning, M.F., Curcio-Morelli, C., Varro, A., Michaud, N., Nanthakumar, N., Walkley, S.U., Pickel, J. and Slaugenhaupt, S.A. (2007) Neurologic, gastric, and opthalmologic pathologies in a murine model of mucolipidosis type IV. *Am. J. Hum. Genet.*, **81**, 1070–1083.
18. Rossi, D. (2015) Astrocyte physiopathology: at the crossroads of intercellular networking, inflammation and cell death. *Prog. Neurobiol.*, **130**, 86–120.
19. Sofroniew, M.V. (2015) Astrocyte barriers to neurotoxic inflammation. *Nat. Rev. Neurosci.*, **16**, 249–263.
20. Chen, G., Li, H.M., Chen, Y.R., Gu, X.S. and Duan, S. (2007) Decreased estradiol release from astrocytes contributes to the neurodegeneration in a mouse model of Niemann-Pick disease type C. *Glia*, **55**, 1509–1518.
21. Di Malta, C., Fryer, J.D., Settembre, C. and Ballabio, A. (2012) Astrocyte dysfunction triggers neurodegeneration in a lysosomal storage disorder. *Proc. Natl. Acad. Sci. U.S.A.*, **109**, E2334–E2342.
22. Di Malta, C., Fryer, J.D., Settembre, C. and Ballabio, A. (2012) Autophagy in astrocytes: a novel culprit in lysosomal storage disorders. *Autophagy*, **8**, 1871–1872.
23. Parviainen, L., Dihanich, S., Anderson, G.W., Wong, A.M., Brooks, H.R., Abeti, R., Rezaie, P., Lalli, G., Pope, S., Heales, S.J. *et al.* (2017) Glial cells are functionally impaired in juvenile neuronal ceroid lipofuscinosis and detrimental to neurons. *Acta Neuropathol.*, **5**, 74.

24. Brunkhorst, R., Vutukuri, R. and Pfeilschifter, W. (2014) Fingolimod for the treatment of neurological diseases-state of play and future perspectives. *Front. Cell. Neurosci.*, **8**, 283.
25. Eriksson, L., Johansson, E., Kettaneh-Wold, N. and Wold, S. (2006) Multi-and Megavariate Data Analysis. Umetrics, Umeå.
26. Wood, L.B., Winslow, A.R., Proctor, E.A., McGuone, D., Mordes, D.A., Frosch, M.P., Hyman, B.T., Lauffenburger, D.A. and Haigis, K.M. (2015) Identification of neurotoxic cytokines by profiling Alzheimer's disease tissues and neuron culture viability screening. *Sci. Rep.*, **5**, 16622.
27. Tzartos, J.S., Friese, M.A., Craner, M.J., Palace, J., Newcombe, J., Esiri, M.M. and Fugger, L. (2008) Interleukin-17 production in central nervous system-infiltrating T cells and glial cells is associated with active disease in multiple sclerosis. *Am. J. Pathol.*, **172**, 146–155.
28. Mills Ko, E., Ma, J.H., Guo, F., Miers, L., Lee, E., Bannerman, P., Burns, T., Ko, D., Sohn, J., Soulika, A.M. *et al.* (2014) Deletion of astroglial CXCL10 delays clinical onset but does not affect progressive axon loss in a murine autoimmune multiple sclerosis model. *J. Neuroinflam.*, **11**, 105.
29. Parajuli, B., Horiuchi, H., Mizuno, T., Takeuchi, H. and Suzumura, A. (2015) CCL11 enhances excitotoxic neuronal death by producing reactive oxygen species in microglia. *Glia*, **63**, 2274–2284.
30. Phares, T.W., Stohlman, S.A., Hinton, D.R. and Bergmann, C.C. (2013) Astrocyte-derived CXCL10 drives accumulation of antibody-secreting cells in the central nervous system during viral encephalomyelitis. *J. Virol.*, **87**, 3382–3392.
31. Wu, F., Zhao, Y., Jiao, T., Shi, D., Zhu, X., Zhang, M., Shi, M. and Zhou, H. (2015) CXCR2 is essential for cerebral endothelial activation and leukocyte recruitment during neuroinflammation. *J. Neuroinflam.*, **12**, 98.
32. Zhang, Z.J., Cao, D.L., Zhang, X., Ji, R.R. and Gao, Y.J. (2013) Chemokine contribution to neuropathic pain: respective induction of CXCL1 and CXCR2 in spinal cord astrocytes and neurons. *Pain*, **154**, 2185–2197.
33. Ma, X., Reynolds, S.L., Baker, B.J., Li, X., Benveniste, E.N. and Qin, H. (2010) IL-17 enhancement of the IL-6 signaling cascade in astrocytes. *J. Immunol.*, **184**, 4898–4906.
34. Chai, Q., She, R., Huang, Y. and Fu, Z.F. (2015) Expression of neuronal CXCL10 induced by rabies virus infection initiates infiltration of inflammatory cells, production of chemokines and cytokines, and enhancement of blood–brain barrier permeability. *J. Virol.*, **89**, 870–876.
35. Imaizumi, T., Sakashita, N., Mushiga, Y., Yoshida, H., Hayakari, R., Xing, F., Wang, L., Matsumiya, T., Tanji, K., Chiba, Y. *et al.* (2015) Desferrioxamine, an iron chelator, inhibits CXCL10 expression induced by polyinosinic-polycytidylic acid in U373MG human astrocytoma cells. *Neurosci. Res.*, **94**, 10–16.
36. Zimmermann, J., Emrich, M., Krauthausen, M., Saxe, S., Nitsch, L., Heneka, M.T., Campbell, I.L. and Muller, M. (2017) IL-17A promotes granulocyte infiltration, myelin loss, microglia activation, and behavioral deficits during cuprizone-induced demyelination. *Mol. Neurobiol.*, **55**, 946–957.
37. Yu, A., Duan, H., Zhang, T., Pan, Y., Kou, Z., Zhang, X., Lu, Y., Wang, S. and Yang, Z. (2016) IL-17A promotes microglial activation and neuroinflammation in mouse models of intracerebral haemorrhage. *Mol. Immunol.*, **73**, 151–157.
38. Li, Y.N., Pan, R., Qin, X.J., Yang, W.L., Qi, Z., Liu, W. and Liu, K.J. (2014) Ischemic neurons activate astrocytes to disrupt endothelial barrier via increasing VEGF expression. *J. Neurochem.*, **129**, 120–129.
39. Shen, S.W., Duan, C.L., Chen, X.H., Wang, Y.Q., Sun, X., Zhang, Q.W., Cui, H.R. and Sun, F.Y. (2016) Neurogenic effect of VEGF is related to increase of astrocytes transdifferentiation into new mature neurons in rat brains after stroke. *Neuropharmacology*, **108**, 451–461.
40. Zhang, Y., Zhai, Q., Luo, Y. and Dorf, M.E. (2002) RANTES-mediated chemokine transcription in astrocytes involves activation and translocation of p90 ribosomal S6 protein kinase (RSK). *J. Biol. Chem.*, **277**, 19042–19048.
41. Janes, K.A., Kelly, J.R., Gaudet, S., Albeck, J.G., Sorger, P.K. and Lauffenburger, D.A. (2004) Cue-signal-response analysis of TNF-induced apoptosis by partial least squares regression of dynamic multivariate data. *J. Comput. Biol.*, **11**, 544–561.
42. Medina, D.L., Settembre, C. and Ballabio, A. (2017) Methods to monitor and manipulate TFEB activity during autophagy. *Methods Enzymol.*, **588**, 61–78.
43. Love, M.I., Huber, W. and Anders, S. (2014) Moderated estimation of fold change and dispersion for RNA-seq data with DESeq2. *Genome Biol.*, **15**, 550.
44. Subramanian, A., Tamayo, P., Mootha, V.K., Mukherjee, S., Ebert, B.L., Gillette, M.A., Paulovich, A., Pomeroy, S.L., Golub, T.R., Lander, E.S. *et al.* (2005) Gene set enrichment analysis: a knowledge-based approach for interpreting genome-wide expression profiles. *Proc. Natl. Acad. Sci. U.S.A.*, **102**, 15545–15550.
45. Patmanathan, S.N., Wang, W., Yap, L.F., Herr, D.R. and Paterson, I.C. (2017) Mechanisms of sphingosine 1-phosphate receptor signalling in cancer. *Cell. Signal.*, **34**, 66–75.
46. Brunkhorst, R., Kanaan, N., Koch, A., Ferreiros, N., Mirceska, A., Zeiner, P., Mittelbronn, M., Derouiche, A., Steinmetz, H., Foerch, C. *et al.* (2013) FTY720 treatment in the convalescence period improves functional recovery and reduces reactive astrogliosis in photothrombotic stroke. *PLoS One*, **8**, e70124.
47. Choi, J.W., Gardell, S.E., Herr, D.R., Rivera, R., Lee, C.W., Noguchi, K., Teo, S.T., Yung, Y.C., Lu, M., Kennedy, G. *et al.* (2011) FTY720 (fingolimod) efficacy in an animal model of multiple sclerosis requires astrocyte sphingosine 1-phosphate receptor 1 (S1P1) modulation. *Proc. Natl. Acad. Sci. U.S.A.*, **108**, 751–756.
48. Wu, C., Leong, S.Y., Moore, C.S., Cui, Q.L., Gris, P., Bernier, L.P., Johnson, T.A., Seguela, P., Kennedy, T.E., Bar-Or, A. *et al.* (2013) Dual effects of daily FTY720 on human astrocytes in vitro: relevance for neuroinflammation. *J. Neuroinflam.*, **10**, 41.
49. Campbell, E.M. and Fares, H. (2010) Roles of CUP-5, the Caenorhabditis elegans orthologue of human TRPML1, in lysosome and gut granule biogenesis. *BMC Cell Biol.*, **11**, 40.
50. Curcio-Morelli, C., Charles, F.A., Micsenyi, M.C., Cao, Y., Venugopal, B., Browning, M.F., Dobrenis, K., Cotman, S.L., Walkley, S.U. and Slaugenhaupt, S.A. (2010) Macroautophagy is defective in mucolipin-1-deficient mouse neurons. *Neurobiol. Dis.*, **40**, 370–377.
51. Grishchuk, Y., Stember, K.G., Matsunaga, A., Olivares, A.M., Cruz, N.M., King, V.E., Humphrey, D.M., Wang, S.L., Muzikansky, A., Betensky, R.A. *et al.* (2016) Retinal dystrophy and optic nerve pathology in the mouse model of mucolipidosis IV. *Am. J. Pathol.*, **186**, 199–209.
52. Micsenyi, M.C., Dobrenis, K., Stephney, G., Pickel, J., Vanier, M.T., Slaugenhaupt, S.A. and Walkley, S.U. (2009) Neuropathology of the Mcoln1($^{-/-}$) knockout mouse model

of mucolipidosis type IV. *J. Neuropathol. Exp. Neurol.*, **68**, 125–135.
53. Ben Haim, L., Carrillo-de Sauvage, M.-A., Ceyzériat, K. and Escartin, C. (2015) Elusive roles for reactive astrocytes in neurodegenerative diseases. *Front. Cell. Neurosci.*, **9**, 278.
54. Glass, C.K., Saijo, K., Winner, B., Marchetto, M.C. and Gage, F.H. (2010) Mechanisms underlying inflammation in neurodegeneration. *Cell*, **140**, 918–934.
55. Semple, B.D., Frugier, T. and Morganti-Kossmann, M.C. (2010) CCL2 modulates cytokine production in cultured mouse astrocytes. *J. Neuroinflam.*, **7**, 67.
56. Thompson, W.L. and Van Eldik, L.J. (2009) Inflammatory cytokines stimulate the chemokines CCL2/MCP-1 and CCL7/MCP-3 through NFkB and MAPK dependent pathways in rat astrocytes [corrected]. *Brain Res.*, **1287**, 47–57.
57. Groh, J., Heinl, K., Kohl, B., Wessig, C., Greeske, J., Fischer, S. and Martini, R. (2010) Attenuation of MCP-1/CCL2 expression ameliorates neuropathy in a mouse model for Charcot-Marie-Tooth 1X. *Hum. Mol. Genet.*, **19**, 3530–3543.
58. Kohl, B., Fischer, S., Groh, J., Wessig, C. and Martini, R. (2010) MCP-1/CCL2 modifies axon properties in a PMP22-overexpressing mouse model for Charcot-Marie-tooth 1A neuropathy. *Am. J. Pathol.*, **176**, 1390–1399.
59. Peferoen, L.A.N., Vogel, D.Y.S., Ummenthum, K., Breur, M., Heijnen, P.D.A.M., Gerritsen, W.H., Peferoen-Baert, R.M.B., van der Valk, P., Dijkstra, C.D. and Amor, S. (2015) Activation status of human microglia is dependent on lesion formation stage and remyelination in multiple sclerosis. *J. Neuropathol. Exp. Neurol.*, **74**, 48–63.
60. Gao, F., Liu, Y., Li, X., Wang, Y., Wei, D. and Jiang, W. (2012) Fingolimod (FTY720) inhibits neuroinflammation and attenuates spontaneous convulsions in lithium-pilocarpine induced status epilepticus in rat model. *Pharmacol. Biochem. Behav.*, **103**, 187–196.
61. van Doorn, R., Nijland, P.G., Dekker, N., Witte, M.E., Lopes-Pinheiro, M.A., van het Hof, B., Kooij, G., Reijerkerk, A., Dijkstra, C., van van der Valk, P., van Horssen, J. and de Vries, H.E. (2012) Fingolimod attenuates ceramide-induced blood–brain barrier dysfunction in multiple sclerosis by targeting reactive astrocytes. *Acta Neuropathol.*, **124**, 397–410.
62. Hoffmann, F.S., Hofereiter, J., Rübsamen, H., Melms, J., Schwarz, S., Faber, H., Weber, P., Pütz, B., Loleit, V., Weber, F. *et al.* (2015) Fingolimod induces neuroprotective factors in human astrocytes. *J. Neuroinflam.*, **12**, 184.
63. Hunter, S.F., Bowen, J.D. and Reder, A.T. (2016) The direct effects of fingolimod in the central nervous system: implications for relapsing multiple sclerosis. *CNS Drugs*, **30**, 135–147.
64. Strub, G.M., Maceyka, M., Hait, N.C., Milstien, S. and Spiegel, S. (2010) Extracellular and intracellular actions of sphingosine-1-phosphate. *Adv. Exp. Med. Biol.*, **688**, 141–155.
65. Gao, C., Qian, Y., Huang, J., Wang, D., Su, W., Wang, P., Guo, L., Quan, W., An, S., Zhang, J. *et al.* (2017) A three-day consecutive fingolimod administration improves neurological functions and modulates multiple immune responses of CCI mice. *Mol. Neurobiol.*, **54**, 8348–8360.
66. Huber, L.A. and Teis, D. (2016) Lysosomal signaling in control of degradation pathways. *Curr. Opin. Cell Biol.*, **39**, 8–14.
67. Onyenwoke, R.U., Sexton, J.Z., Yan, F., Diaz, M.C., Forsberg, L.J., Major, M.B. and Brenman, J.E. (2015) The mucolipidosis IV Ca2+ channel TRPML1 (MCOLN1) is regulated by the TOR kinase. *Biochem. J.*, **470**, 331–342.
68. Wang, W., Gao, Q., Yang, M., Zhang, X., Yu, L., Lawas, M., Li, X., Bryant-Genevier, M., Southall, N.T., Marugan, J. *et al.* (2015) Up-regulation of lysosomal TRPML1 channels is essential for lysosomal adaptation to nutrient starvation. *Proc. Natl. Acad. Sci. U.S.A.*, **112**, E1373–E1381.
69. Xu, H. and Ren, D. (2015) Lysosomal physiology. *Annu. Rev. Physiol.*, **77**, 57–80.
70. Zhang, X., Cheng, X., Yu, L., Yang, J., Calvo, R., Patnaik, S., Hu, X., Gao, Q., Yang, M., Lawas, M. *et al.* (2016) MCOLN1 is a ROS sensor in lysosomes that regulates autophagy. *Nat. Commun.*, **7**, 12109.
71. Molteni, M. and Rossetti, C. (2017) Neurodegenerative diseases: the immunological perspective. *J. Neuroimmunol.*, **313**, 109–115.
72. Ransohoff, R.M., Schafer, D., Vincent, A., Blachere, N.E. and Bar-Or, A. (2015) Neuroinflammation: ways in which the immune system affects the brain. *Neurotherapeutics*, **12**, 896–909.
73. Groh, J., Berve, K. and Martini, R. (2017) Fingolimod and teriflunomide attenuate neurodegeneration in mouse models of neuronal ceroid lipofuscinosis. *Mol. Ther.*, **25**, 1889–1899.
74. Groh, J. and Martini, R. (2017) Neuroinflammation as modifier of genetically caused neurological disorders of the central nervous system: understanding pathogenesis and chances for treatment. *Glia*, **65**, 1407–1422.
75. Jaitin, D.A., Kenigsberg, E., Keren-Shaul, H., Elefant, N., Paul, F., Zaretsky, I., Mildner, A., Cohen, N., Jung, S., Tanay, A. *et al.* (2014) Massively parallel single-cell RNA-seq for marker-free decomposition of tissues into cell types. *Science*, **343**, 776–779.
76. Martin, M. (2011) Cutadapt removes adapter sequences from high-throughput sequencing reads. *EMBnet.journal*, **17**, 10–12.
77. Dobin, A., Davis, C.A., Schlesinger, F., Drenkow, J., Zaleski, C., Jha, S., Batut, P., Chaisson, M. and Gingeras, T.R. (2013) STAR: ultrafast universal RNA-seq aligner. *Bioinformatics*, **29**, 15–21.
78. Anders, S., Pyl, P.T. and Huber, W. (2015) HTSeq–a Python framework to work with high-throughput sequencing data. *Bioinformatics*, **31**, 166–169.
79. Mootha, V.K., Lindgren, C.M., Eriksson, K.F., Subramanian, A., Sihag, S., Lehar, J., Puigserver, P., Carlsson, E., Ridderstrale, M., Laurila, E. *et al.* (2003) PGC-1alpha-responsive genes involved in oxidative phosphorylation are coordinately downregulated in human diabetes. *Nat. Genet.*, **34**, 267–273.